nature structural & molecular biology

ARTICLES

https://doi.org/10.1038/s41594-021-00570-0

Structural basis for inhibition of the SARS-CoV-2 RNA polymerase by suramin

Wanchao Yin[1,9], Xiaodong Luan[2,3,4,9], Zhihai Li[1,5,9], Ziwei Zhou[1,5,6,9], Qingxing Wang[6,7,9], Minqi Gao[8], Xiaoxi Wang[1], Fulai Zhou[1], Jingjing Shi[1], Erli You[1], Mingliang Liu[1], Qingxia Wang[1,5], Yi Jiang[1,6], Hualiang Jiang[1,6], Gengfu Xiao[7], Leike Zhang[6,7] ✉, Xuekui Yu[1,5,6] ✉, Shuyang Zhang[2,3,4] ✉ and H. Eric Xu[1,6] ✉

The COVID-19 pandemic caused by nonstop infections of SARS-CoV-2 has continued to ravage many countries worldwide. Here we report that suramin, a 100-year-old drug, is a potent inhibitor of the SARS-CoV-2 RNA-dependent RNA polymerase (RdRp) and acts by blocking the binding of RNA to the enzyme. In biochemical assays, suramin and its derivatives are at least 20-fold more potent than remdesivir, the currently approved nucleotide drug for treatment of COVID-19. The 2.6 Å cryo-electron microscopy structure of the viral RdRp bound to suramin reveals two binding sites. One site directly blocks the binding of the RNA template strand and the other site clashes with the RNA primer strand near the RdRp catalytic site, thus inhibiting RdRp activity. Suramin blocks viral replication in Vero E6 cells, although the reasons underlying this effect are likely various. Our results provide a structural mechanism for a nonnucleotide inhibitor of the SARS-CoV-2 RdRp.

Severe acute respiratory syndrome coronavirus 2 (SARS-CoV-2) has caused a global pandemic of coronavirus disease 2019 (COVID-19), with over 84.66 million infections and 1.83 million deaths as reported on 3 January 2021 (refs. [1,2]). SARS-CoV-2 is a positive-sense, single-stranded RNA virus. SARS-CoV-2 and several related beta-coronaviruses, including SARS-CoV and Middle East respiratory syndrome coronavirus (MERS-CoV), are highly pathogenic. Infections can lead to severe acute respiratory syndrome, loss of lung function and, in severe cases, death. Compared to SARS-CoV and MERS-CoV, SARS-CoV-2 has a higher capacity of human-to-human infections, which resulted in the rapidly growing pandemic[3]. Finding an effective treatment for COVID-19, potentially also through drug repurposing, is an urgent but unmet medical need.

Suramin (Fig. 1a) is a century-old drug that has been used to treat African sleeping sickness and river blindness[4,5]. It has also been shown to be effective in inhibiting the replication of a wide range of viruses, including enteroviruses[6], Zika virus[7], Chikungunya[8] and Ebola viruses[9]. The viral inhibition mechanisms of suramin are diverse, including inhibition of viral attachment, viral entry and release from host cells in part through interactions with viral capsid proteins[7,8,10,11]. Recently, suramin has been shown to inhibit SARS-CoV-2 infection in cell culture by preventing cellular entry of the virus[12]. Here we report that suramin is also a potent inhibitor of the SARS-CoV-2 RNA-dependent RNA polymerase (RdRp), an essential enzyme for the viral life cycle. The potency of suramin in biochemical RdRp inhibition assays is at least 20-fold more potent than remdesivir, the current Food and Drug Administration-approved nucleotide drug for the treatment of COVID-19. The activity of suramin in cell-based viral inhibition is similar to remdesivir because the highly negative charge of suramin prevents efficient cellular uptake. A cryogenic electron microscopy (cryo-EM) structure reveals that suramin binds to the RdRp active site, blocking the binding of both RNA template and primer strands. These results provide a structural template for the design of next generation suramin derivatives as SARS-CoV-2 RdRp inhibitors.

Results

Inhibition of RdRp and anti-SARS-CoV-2 by suramin. The core RNA polymerase of SARS-CoV-2 is composed of nonstructural protein nsp12 with two accessary subunits nsp7 and nsp8 (refs. [13,14]). Incubation of the purified nsp12–7–8 complex (Extended Data Figs. 1a,b) with a 30-base template and 20-base primer (poly-U in Fig. 1b) allowed primer extension to the same length as the template in the presence of saturated concentrations of ATP as illustrated in a gel-based assay (lane 1 in Fig. 1c). Addition of 8–32 μM suramin nearly abolished the elongation of the primer strand while it required 100–1,000 μM of remdesivir in its triphosphate form (RDV-TP) to achieve the same degree of inhibition under the same conditions[15]. Addition of 100 μM suramin completely blocked the formation of RdRp–RNA complex, while it required more than 5 mM of RDV-TP to inhibit the binding of RdRp to RNA (Fig. 1d and Extended Data Fig. 1c). Solution based assays of RdRp inhibition determined that the half-maximal inhibition concentration (IC_{50}) of suramin is 0.26 μM (Fig. 1e), and the IC_{50} for RDV-TP is 6.21 μM under identical assay conditions (Extended Data Fig. 1d), suggesting that suramin is at least 20-fold more potent than RDV-TP. Cell-based experiments indicated that suramin was able to inhibit SARS-CoV-2

[1]The CAS Key Laboratory of Receptor Research, Shanghai Institute of Materia Medica, Chinese Academy of Sciences, Shanghai, China. [2]School of Medicine, Tsinghua University, Haidian District, Beijing, China. [3]Department of Cardiology, Peking Union Medical College Hospital, Peking Union Medical College and Chinese Academy of Medical Sciences, Beijing, China. [4]Tsinghua-Peking Center for Life Sciences, Tsinghua University, Beijing, China. [5]Cryo-Electron Microscopy Research Center, Shanghai Institute of Materia Medica, Chinese Academy of Sciences, Shanghai, China. [6]University of Chinese Academy of Sciences, Beijing, China. [7]State Key Laboratory of Virology, Wuhan Institute of Virology, Center for Biosafety Mega-Science, Chinese Academy of Sciences, Wuhan, Hubei, China. [8]WuxiBiortus Biosciences Co. Ltd, Jiangyin, China. [9]These authors contributed equally: Wanchao Yin, Xiaodong Luan, Zhihai Li, Ziwei Zhou, Qingxing Wang. ✉e-mail: zhangleike@wh.iov.cn; xkyu@simm.ac.cn; shuyangzhang103@nrdrs.org; eric.xu@simm.ac.cn

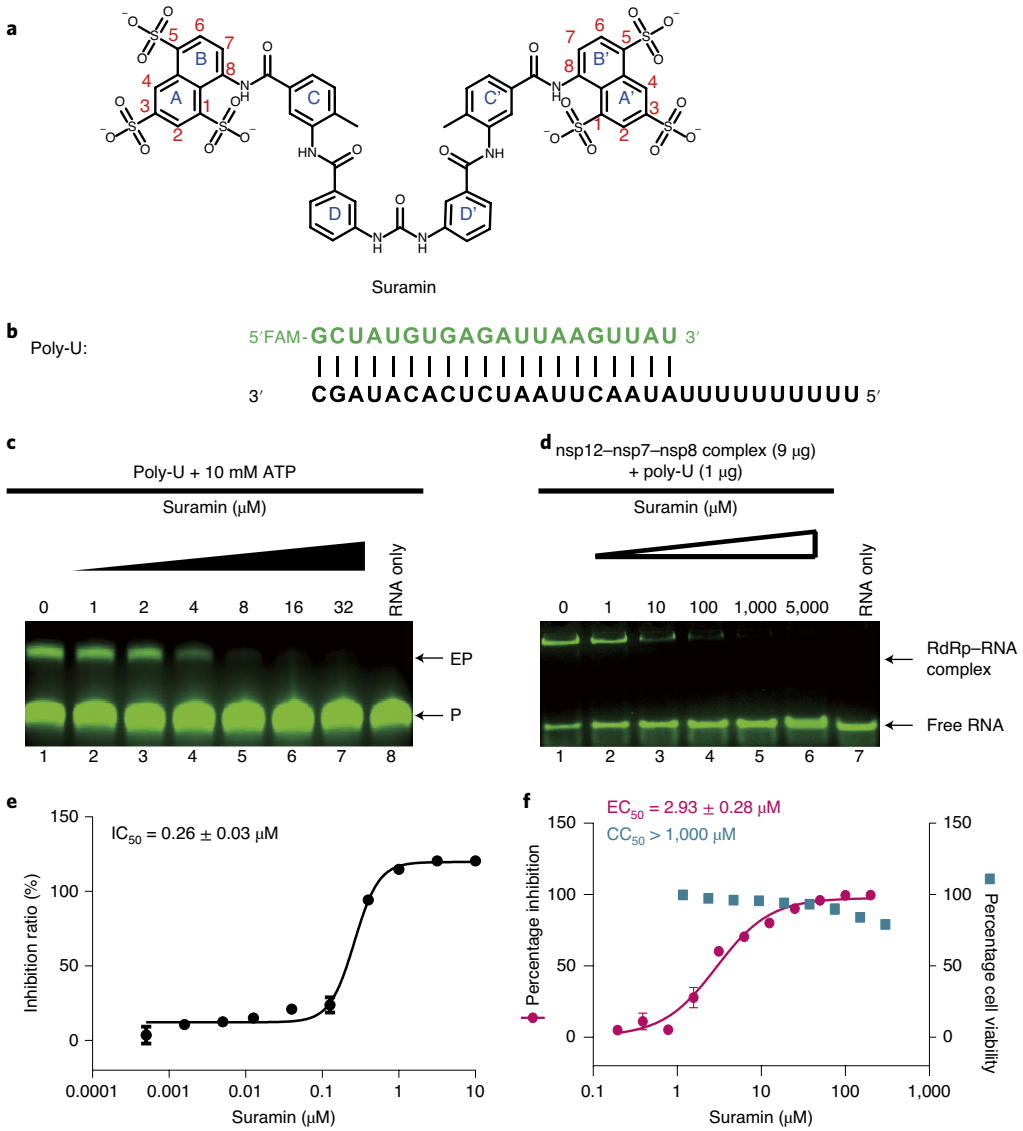

Fig. 1 | Inhibition of RdRp by suramin and the potential anti-SARS-CoV-2 effect of suramin. a, The chemical structure of suramin. **b**, The 30-base template and 20-base primer duplex RNA with FAM (Carboxyfluorescein) at the 5′ of the primer. Poly-U was used in the gel-based elongation assay for SARS-CoV-2 RdRp. **c**, Gel assays of elongation of partial RNA duplex by the purified RdRp complex and its inhibition by suramin. EP, elongated product; P, primer RNA strand. **d**, Gel mobility shift of the RdRp–RNA complex and the effect of suramin. **e**, IC_{50} of suramin for RdRp complex, determined by two independent experiments and error bars are the mean ± s.d. of the data. **f**, EC_{50} of suramin for SARS-CoV-2 inhibition and CC_{50} of suramin for cell-based toxicity, determined by three independent experiments and error bars are the mean ± s.d. of the data. Uncropped images for **c** and **d** and data for the graphs in **e** and **f** are available as source data online.

duplication in Vero E6 cells with a half-maximal effective concentration (EC_{50}) of roughly 2.9 μM, which is about the same range as remdesivir in the same assay (Fig. 1f and Extended Data Fig. 1e)[16]. The apparent weaker inhibition of suramin in cell-based assays than in enzyme inhibition assays may be due to the highly negative charge of suramin that prevent its efficient uptake by the host cells. The CC_{50} (concentrations of drug required to reduce cell viability by 50%) of suramin is over 1,000 μM, indicating that its relatively low cytotoxicity that is lower than that of remdesivir (Fig. 1f and Extended Data Fig. 1e).

The structure of the RdRp–suramin complex. For the cryo-EM studies, we incubated the SARS-CoV-2 RdRp complex with tenfold molar excess of suramin (Methods). The structure was determined at a global resolution of 2.57 Å with 95,845 particles from over 8 million original particles auto-picked from 11,846 micrographs (Extended Data Fig. 2 and Table 1). The EM map reveals clear density for all key components of the RdRp–suramin complex, including one nsp12 (residues S6-C22, V31-I106, M110-L895 and N911-T929), one nsp7 (residues K2-G64), two nsp8 (residues D78-A191 for nsp8-1 and residues T84-A191 for nsp8-2, respectively) and two suramin molecules (Fig. 2a and Extended Data Fig. 3).

The overall structure of the RdRp–suramin complex is very similar to the apo–RdRp complex, with a root mean squared deviation (r.m.s.d.) of 0.465 Å for all Cα atoms between the two structures (Fig. 2b and Extended Data Fig. 4a). The core RdRp complex structure is also very similar to the recently solved core RdRp complex with nsp13 and nsp9 or nsp13 (refs. [17–19]) (Extended Data Fig. 4b–d). Nsp12 adopts the same right-hand palm fingers configuration, with its catalytic active site composed of seven highly conserved motifs

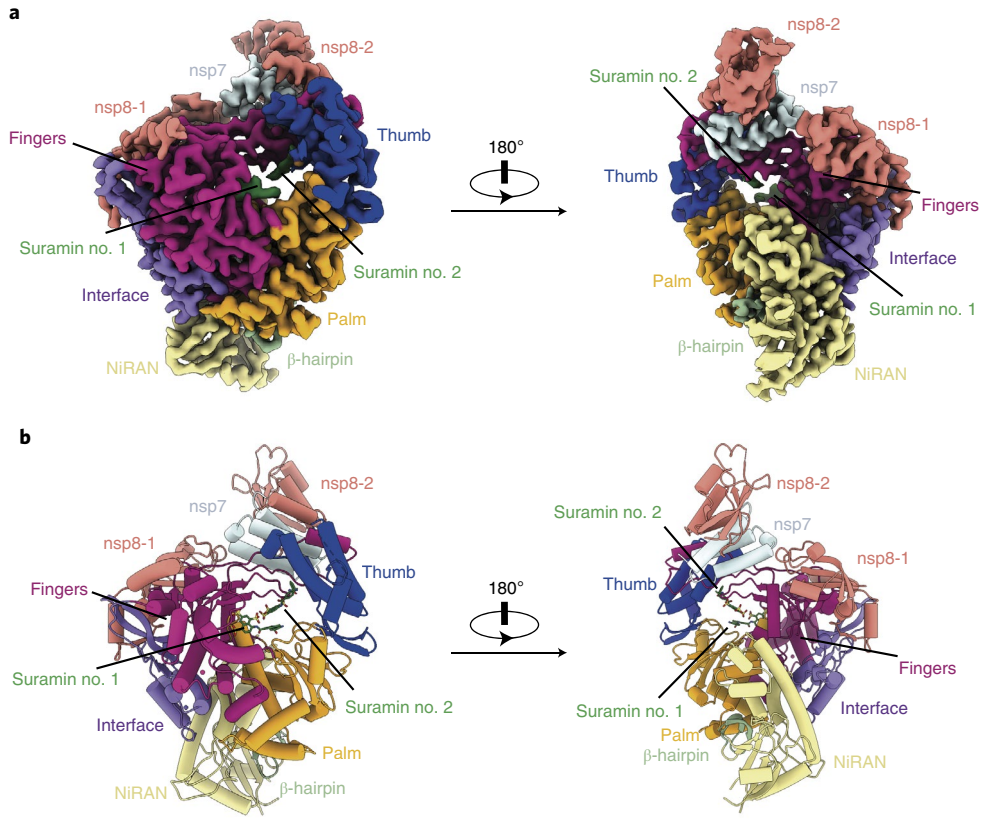

Fig. 2 | Overall structures of the RdRp–suramin complex. a, Two views of the cryo-EM density map of the RdRp–suramin complex. SARS-CoV-2 nsp12 has an N-terminal extension composed of the β-hairpin (green), the NiRAN domain (yellow) and an interface domain (purple) adjacent to the RdRp core domain, which consists of the following subdomains: fingers, palm and thumb, colored violet, orange and blue, respectively. Nsp12 binds to a heterodimer of nsp7 (light green) and nsp8 (nsp8-2, red) as well as to a second subunit of nsp8 (nsp8-1, red). The two bound suramin molecules are set in dark green. This color code is used throughout. **b**, Two views of the overall structure of the RdRp–suramin complex, the color scheme is as above.

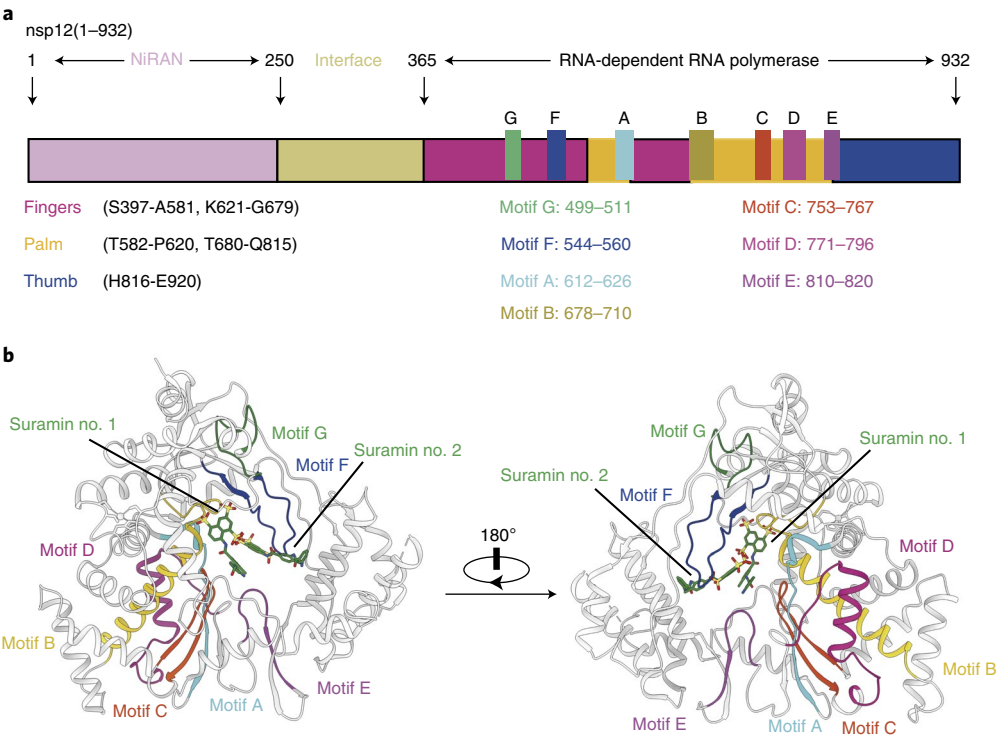

Fig. 3 | The conserved motifs A–G in the RdRp–suramin complex. a, Schematic diagram of the RdRp complex subunit nsp12; motifs A to G are highlighted. **b**, Interactions of the two suramin molecules with motifs A–G of RdRp. The color code is as follows: motif A (cyan), motif B (gold), motif C (orange red), motif D (medium violet red), motif E (magenta), motif F (blue) and motif G (green).

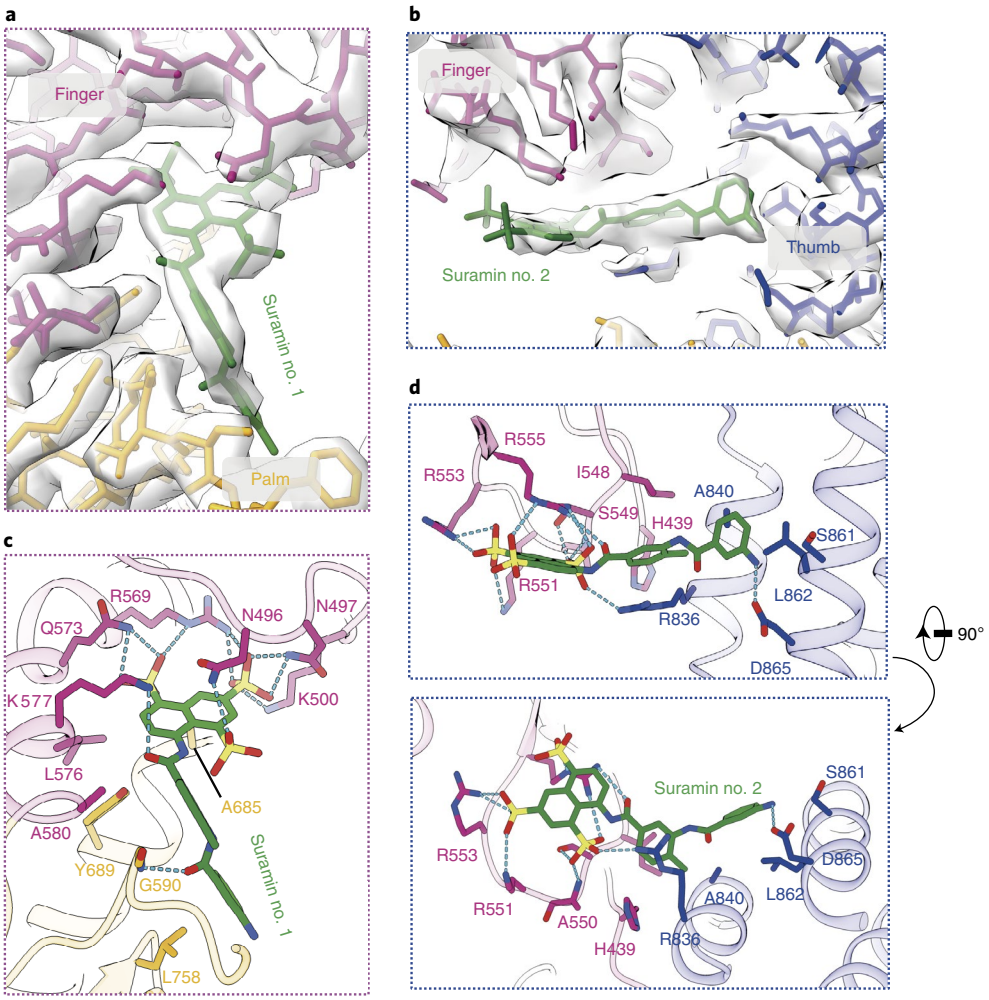

Fig. 4 | Close views of the interactions between the SARS-CoV-2 RdRp and suramin. a,**b**, EM maps for the two suramin molecules: no. 1 (**a**) and no. 2 (**b**). **c**,**d**, Interactions of the two suramin molecules with RdRp: no. 1 (**c**) and no. 2 (**d**). The hydrogen bond is displayed as a blue dashed line.

A–G (Fig. 3a). Two suramin molecules fit into the catalytic chamber (Figs. 2a,b and 3b).

The interactions of suramin with SARS-CoV-2 RdRp. One suramin molecule (suramin no. 1) is fit into a cavity formed by a conserved motif G and the N terminus of motif B (Figs. 3b and 4a). The chemical structure of suramin has a twofold symmetry with a urea linker at the center (Fig. 1a). The EM density map for suramin no. 1 is clearly defined but only for half of the suramin molecule without the urea linker (Fig. 4a,b). The key interactions of suramin no. 1 with RdRp were summarized in Fig. 4c and Supplementary Table 1, including hydrogen bonds, charge interactions and hydrophobic packing interactions with conserved RdRp residues, which restrain the naphthalene-trisulfonic acid head in a relative narrow cavity. Two out of the three sulfonates (positions 3 and 5) form hydrogen bonds with the side chains from N497, K500, R569 and Q573, and the main chain from N497, while the sulfonate at position 1 points toward the solvent and forms only one hydrogen bond with the side chain of N496. The K577 side chain forms cation–π stacking with the naphthalene ring, and also forms a hydrogen bond with the amide bond linker between the naphthalene and benzene rings. The amide bond linker between the benzene rings C and D forms a hydrogen bond with main chain NH of G590. In addition, suramin no. 1 is in van der Waals contact with several residues, including L576, A580, A685, Y689 and L758. The second suramin molecule (suramin no. 2) is fit into the cavity near the catalytic active site formed by conserved motifs A, C, E and F (Figs. 3b and 4b). Again, only half of the molecule was observed in the structure with clear EM density map. The key interactions of suramin no. 2 with RdRp are summarized in Fig. 4d and Supplementary Table 1, including hydrogen bonds, charge interactions and hydrophobic packing interactions. Different from suramin no. 1, the sulfonate at position 5 of suramin no. 2 points toward the solvent and forms only one hydrogen bond with the side chain of R555, while the other two sulfonates at positions 1 and 3 form hydrogen bonds with the side chains from K551, R553, R555 and R836, and the main chains from A550 and K551. Meanwhile the side chain of R555 also forms a hydrogen bond with the amide bond linker between the naphthalene and benzene rings. The R836 side chain forms cation–π stacking with the benzene ring C. The NH of the benzene ring D forms a hydrogen bond with the side chain of D865. In addition, suramin no. 2 is in van der Waals contact with several residues, including H439, I548, S549, A840, S861 and L862. Sequence alignment with RdRp from several coronaviruses indicated that these suramin-contacting residues are conserved (Supplementary Fig. 1), suggesting that suramin may be a general inhibitor of viral RdRp.

Inhibition mechanism of suramin toward SARS-CoV-2 RdRp. Structural comparison of the RdRp–suramin complex with the remdesivir-bound RdRp complex reveals the mechanism of RdRp inhibition by suramin (Fig. 5a). If the base position of remdesivir was defined as a +1 position, then the first suramin molecule occupies the space of −1 to −3 positions of the RNA template

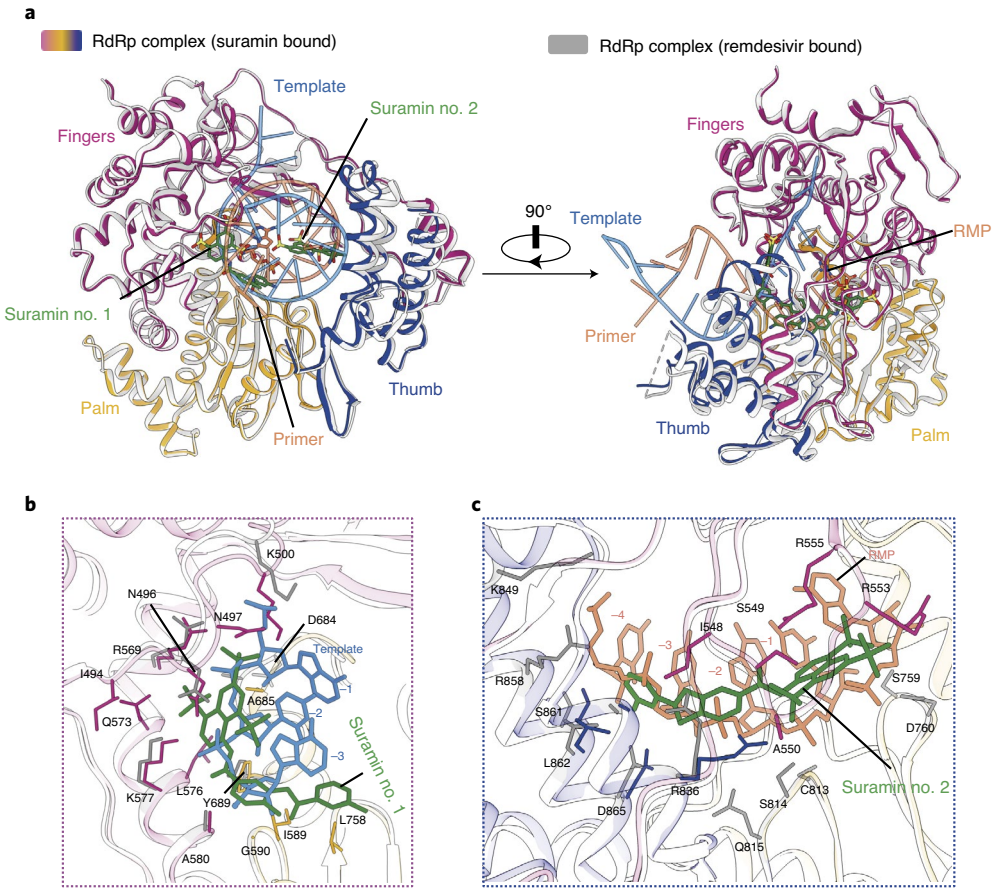

Fig. 5 | Inhibition mechanism from comparison with the remdesivir-bound RdRp structure. a, Overall views of the RdRp–suramin complex overlapped with the remdesivir-bound RdRp structure (PDB ID 7BV2). For clarity, only the polymerase domains are presented. The remdesivir-bound RdRp structure is shown in light gray, the template RNA is cyan and the primer RNA is orange. **b**, Close view of suramin no. 1 overlapped with RNA template strand from the remdesivir-bound RdRp structure. **c**, Close view of suramin no. 2 overlapped with the RNA primer strand from the remdesivir-bound RdRp structure.

strand (suramin no. 1 in Fig. 5b). The second suramin molecule at the active site occupies the space of the primer strand ranging from −4 to +1 positions (suramin no. 2 in Fig. 5c). The binding of these two suramin molecules thus blocks the binding of the RNA template–primer duplex to the active site as well as the entry of nucleotide triphosphate into the catalytic site, which would result in the direct inhibition of the RdRp catalytic activity. The direct inhibition mechanism of SARS-CoV-2 RdRp by suramin is different from the suramin-mediated inhibition of the norovirus RdRp, which also contained two binding sites for suramin[20]. In each site, only half of suramin molecule was seen. Structural comparison of the SARS-CoV-2 RdRp with the norovirus RdRp reveals that only one of the two suramin binding sites (suramin no. 2) partially overlapped (Extended Data Fig. 5a,c,d). The suramin binding sites in norovirus RdRp do not clash with the RNA strands but one of the suramin binding site overlapped with the proposed nucleotide entry channel, thus indirectly blocking RdRp polymerization activity. This mechanism is different from the direct block of the binding of the RNA template to the SARS-CoV-2 RdRp by suramin (Fig. 5). In addition, structural comparisons of the SARS-CoV-2 RdRp–suramin structure with the structures of the norovirus RdRp bound to suramin derivatives show that suramin and suramin derivatives bind to the RdRp with diverse conformations and orientations[20,21] (Extended Data Figs. 5b,e and 6).

Inhibition SARS-CoV-2 RdRp by suramin derivatives. Suramin derivatives have been explored for diverse applications, including parasitic diseases and cancer[10]. To determine the structure–activity relationship for suramin derivatives, we screened a set of different ones using in vitro RdRp primer extension assays (Fig. 6a and Extended Data Fig. 1f). All eight tested suramin derivatives showed efficient inhibition of RdRp activity (Extended Data Fig. 1g). NF157, NF279 and NF449 are the most potent inhibitors with IC_{50} of 0.05 μM, about fivefold more potent than the parent drug (Fig. 6b). Cell-based assays showed that NF110 inhibited SARS-CoV-2 replication with an EC_{50} of 2.87 μM (Fig. 6c), while NF157 and NF279 inhibited SARS-CoV-2 replication with EC_{50} of roughly 10 μM. The CC_{50} values of all suramin derivatives are over 1,000 μM, indicating a good safety window. However, there is a 200-fold separation between their biochemical potency in inhibiting RdRp activity and their potency in inhibiting viral replication in cell-based assays. This is likely due to difficulties of these suramin derivatives to be taken up by host cells[22]. Future drug formulation, for example with glycol chitosan-based nanoparticles[23], may improve their bioavailability to lung tissues and their potency in inhibiting viral replication.

Discussion

The current COVID-19 pandemic evidences the need for effective vaccines and drug treatments for the disease. Suramin has been used to treat African sleeping sickness and that has also shown activity against a number of viruses in preclinical studies. In addition, suramin was shown to block SARS-CoV-2 at an earlier step of the replication cycle in time-of-addition assays[12]. Here, we demonstrate that suramin is a direct and potent inhibitor of the SARS-CoV-2 RdRp,

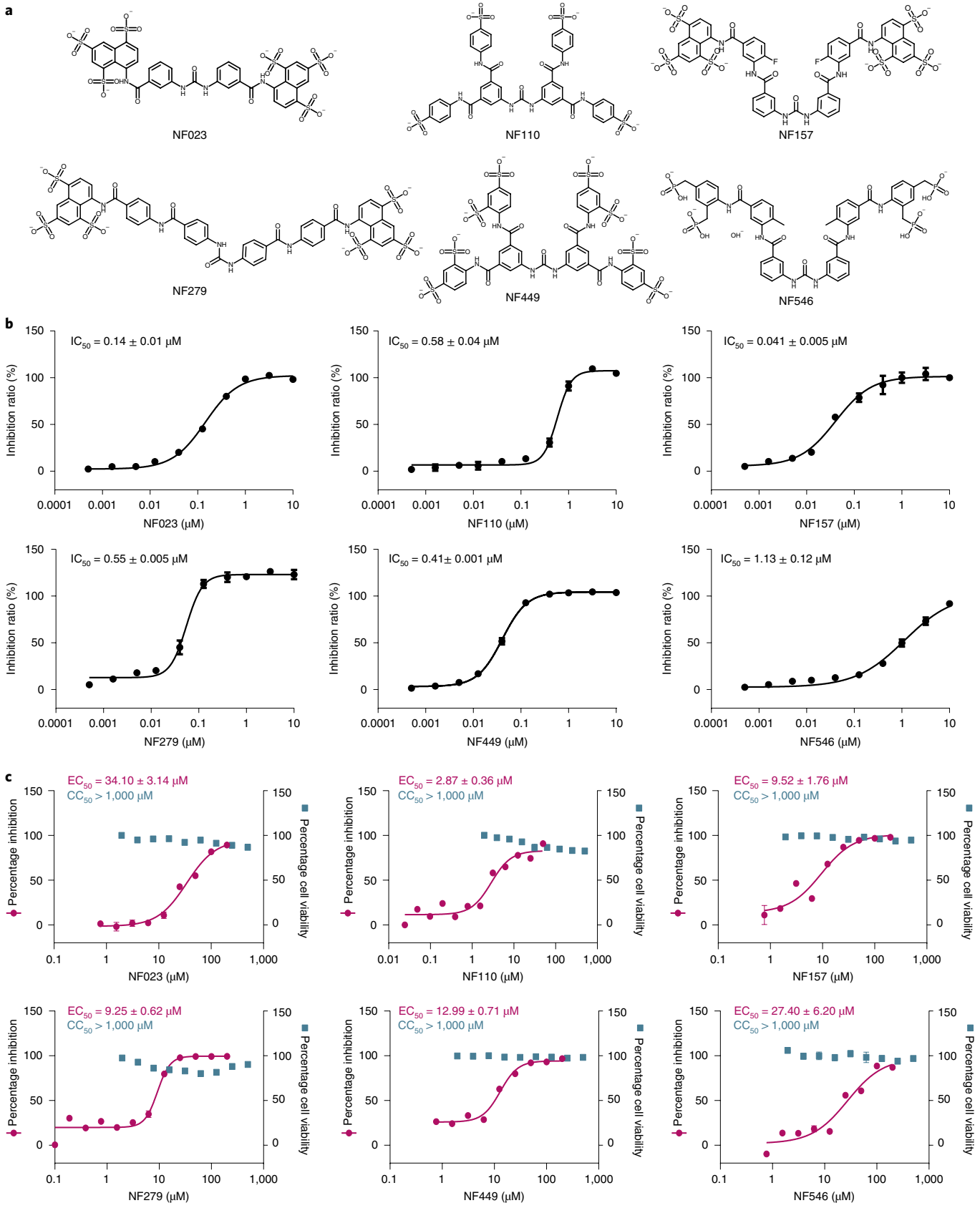

Fig. 6 | Inhibition SARS-CoV-2 RdRp by suramin derivatives. a, Chemical structures of suramin derivatives. **b**, The inhibition of RdRp activity by suramin derivatives, determined by two independent experiments and error bars showing the mean ± s.d. of the data. **c**, Inhibition of viral replication and cellular toxicity of suramin derivatives, determined by three independent experiments and error bars showing the mean ± s.d. of the data. Source data for **b** and **c** are available online.

Table 1 | Cryo-EM data collection, refinement and validation statistics

	SARS-CoV-2 RdRp–suramin complex (EMD-30572, PDB 7D4F)
Data collection and processing	
Magnification	46,773
Voltage (kV)	300
Electron exposure (e^-/Å^2)	68
Defocus range (μm)	−0.5 to −2.0
Pixel size (Å)	1.069
Symmetry imposed	*C*1
Initial particle images (no.)	8,557,180
Final particle images (no.)	95,845
Map resolution (Å)	2.6
FSC threshold	0.143
Map resolution range (Å)	2.5–6.0
Refinement	
Initial model used	7BV1
Model resolution (Å)	2.7
FSC threshold	0.5
Model resolution range (Å)	28.0–2.7
Map sharpening *B* factor (Å^2)	−27.866
Model composition	
Nonhydrogen atoms	9,534
Protein residues	1,181
Ligands	4
B factors (Å^2)	
Protein	63.49
Ligand	64.64
R.m.s. deviations	
Bond lengths (Å)	0.012
Bond angles (°)	0.904
Validation	
MolProbity score	1.34
Clashscore	5.43
Poor rotamers (%)	0.76
Ramachandran plot	
Favored (%)	97.77
Allowed (%)	2.23
Disallowed (%)	0

an essential enzyme for the viral life cycle. The structure reveals that suramin binds to the active site of RdRp, blocking the binding of both strands of the template–primer RNA substrate and inhibiting the polymerase activity of the RdRp. Suramin derivatives also showed potent inhibition of RdRp activity and blocked viral replication in cell-based assays. Together, these results uncover the structural mechanism of a nonnucleotide inhibitor of the SARS-CoV-2 RdRp. The structure and biochemical results presented in this paper provide a rationale to develop suramin analogs and drug formulations that improve potency and efficacy of the drug. However, there are a number of limitations of suramin, including its high negative charge, which hinders its efficient entry into cell. In addition, there are potential risks of off-target effects on cellular polymerases and helicases. Nevertheless, suramin can serve as an interesting 'tool compound' for fundamental mechanistic studies into the viral RdRp, which could ultimately aid in drug development for COVID-19.

Online content

Any methods, additional references, Nature Research reporting summaries, source data, extended data, supplementary information, acknowledgements, peer review information; details of author contributions and competing interests; and statements of data and code availability are available at https://doi.org/10.1038/s41594-021-00570-0.

Received: 28 October 2020; Accepted: 5 February 2021;
Published online: 5 March 2021

References

1. Coronaviridae Study Group of the International Committee on Taxonomy of Viruses. The species severe acute respiratory syndrome-related coronavirus: classifying 2019-nCoV and naming it SARS-CoV-2. *Nat. Microbiol.* **5**, 536–544 (2020).
2. Dong, E., Du, H. & Gardner, L. An interactive web-based dashboard to track COVID-19 in real time. *Lancet Infect. Dis.* **20**, 533–534 (2020).
3. Sanche, S. et al. High contagiousness and rapid spread of Severe Acute Respiratory Syndrome Coronavirus 2. *Emerg. Infect. Dis.* **26**, 1470–1477 (2020).
4. Brun, R., Blum, J., Chappuis, F. & Burri, C. Human African trypanosomiasis. *Lancet* **375**, 148–159 (2010).
5. Hawking, F. Symposium on onchocerciasis III. Chemotherapy of onchocerciasis. *Trans. R. Soc. Tropical Med. Hyg.* **52**, 109–111 (1958).
6. Ren, P. et al. The approved pediatric drug suramin identified as a clinical candidate for the treatment of EV71 infection-suramin inhibits EV71 infection in vitro and in vivo. *Emerg. Microbes Infect.* **3**, e62 (2014).
7. Albulescu, I. C., Kovacikova, K., Tas, A., Snijder, E. J. & van Hemert, M. J. Suramin inhibits Zika virus replication by interfering with virus attachment and release of infectious particles. *Antivir. Res* **143**, 230–236 (2017).
8. Albulescu, I. C. et al. Suramin inhibits Chikungunya virus replication through multiple mechanisms. *Antivir. Res* **121**, 39–46 (2015).
9. Henss, L. et al. Suramin is a potent inhibitor of Chikungunya and Ebola virus cell entry. *Virol. J.* **13**, 149 (2016).
10. Wiedemar, N., Hauser, D. A. & Maser, P. 100 years of suramin. *Antimicrob. Agents Chemother.* **64**, e01168–19 (2020).
11. Albulescu, I. C. et al. Suramin inhibits Chikungunya virus replication by interacting with virions and blocking the early steps of infection. *Viruses* **12**, 314 (2020).
12. Salgado-Benvindo, C. et al. Suramin inhibits SARS-CoV-2 infection in cell culture by interfering with early steps of the replication cycle. *Antimicrob. Agents Chemother.* **64**, e00900–20 (2020).
13. Subissi, L. et al. One severe acute respiratory syndrome coronavirus protein complex integrates processive RNA polymerase and exonuclease activities. *Proc. Natl Acad. Sci. USA* **111**, E3900–E3909 (2014).
14. Kirchdoerfer, R. N. & Ward, A. B. Structure of the SARS-CoV nsp12 polymerase bound to nsp7 and nsp8 co-factors. *Nat. Commun.* **10**, 2342 (2019).
15. Yin, W. et al. Structural basis for inhibition of the RNA-dependent RNA polymerase from SARS-CoV-2 by remdesivir. *Science* **368**, 1499–1504 (2020).
16. Wang, M. et al. Remdesivir and chloroquine effectively inhibit the recently emerged novel coronavirus (2019-nCoV) in vitro. *Cell Res* **30**, 269–271 (2020).
17. Chen, J. et al. Structural basis for helicase-polymerase coupling in the SARS-CoV-2 replication-transcription complex. *Cell* **182**, 1560–1573 e13 (2020).
18. Yan, L. et al. Cryo-EM structure of an extended SARS-CoV-2 replication and transcription complex reveals an intermediate state in cap synthesis. *Cell* **184**, 184–193 e10 (2021).
19. Yan, L. et al. Architecture of a SARS-CoV-2 mini replication and transcription complex. *Nat. Commun.* **11**, 5874 (2020).
20. Mastrangelo, E. et al. Structure-based inhibition of norovirus RNA-dependent RNA polymerases. *J. Mol. Biol.* **419**, 198–210 (2012).
21. Croci, R. et al. Structural bases of norovirus RNA dependent RNA polymerase inhibition by novel suramin-related compounds. *PLoS ONE* **9**, e91765 (2014).
22. Alsford, S., Field, M. C. & Horn, D. Receptor-mediated endocytosis for drug delivery in African trypanosomes: fulfilling Paul Ehrlich's vision of chemotherapy. *Trends Parasitol.* **29**, 207–212 (2013).
23. Cheng, B., Gao, F., Maissy, E. & Xu, P. Repurposing suramin for the treatment of breast cancer lung metastasis with glycol chitosan-based nanoparticles. *Acta Biomater.* **84**, 378–390 (2019).

Methods

Constructs and expression of the RdRp complex. The RdRp complex was prepared according to same method reported[14] as described below. The full-length gene of the SARS-CoV-2 *nsp12* (encodes residues 1–932) was chemically synthesized with codon optimization (General Biosystems). The gene was cloned into a modified pFastBac baculovirus expression vector containing a 5′ ATG starting sequence and C-terminal tobacco etch virus (TEV) protease site followed by a His8 tag. The plasmid contains an additional methionine at the N terminus and GGSENLYFQGHHHHHHHH at the C terminus of nsp12. The full-length genes for *nsp7* (encodes residues 1–83) and *nsp8* (encodes residues 1–198) were cloned into the pFastBac vector containing a 5′ ATG starting sequence. All constructs were generated using the Phanta Max Super-Fidelity DNA Polymerase (Vazyme Biotech) and verified by DNA sequencing. All constructs were expressed in *Spodoptera frugiperda* (Sf9) cells. Cell cultures were grown in ESF 921 serum-free medium (Expression Systems) to a density of 2–3 million cells per ml and then infected with three separate baculoviruses at a ratio of 1:2:2 for nsp12, nsp7 and nsp8 at a multiplicity of infection of about five. The cells were collected 48 h after infection at 27 °C and cell pellets were stored at −80 °C until use.

In addition, the genes of *nsp7* and *nsp8* were cloned into a modified pET-32a(+) vector containing a 5′ ATG starting sequence and C-terminal His8 tag with a TEV cleavage site for expression in E. coli. Plasmids were transformed into BL21(DE3) (Invitrogen). Bacterial cultures were grown to an OD_{600} of 0.6 at 37 °C, and then the expression was induced with a final concentration of 0.1 mM of isopropyl β-D-1-thiogalactopyranoside and the growth temperature was reduced to 16 °C for 18–20 h. The bacterial cultures were pelleted and stored at −80 °C until use.

Purification of the RdRp complex. The purification of nsp7 and nsp8 expressed in bacteria BL21(DE3) was similar to the purification of nsp7 and nsp8 reported previously[14]. Briefly, bacterial cells were lysed with a high-pressure homogenizer operating at 800 bar. Lysates were cleared by centrifugation at 25,000*g* for 30 min and were then bound to Ni-NTA beads (GE Healthcare). After washing with buffer containing 50 mM imidazole, the protein was eluted with buffer containing 300 mM imidazole. The tag was removed with incubation of TEV protease overnight and protein samples were concentrated with 3 or 30 kDa molecular weight cut-off centrifuge filter units (Millipore Corporation) and then size-separated by a Superdex 75 Increase 10/300 GL column in 25 mM HEPES pH 7.4, 200 mM sodium chloride, 5% (v/v) glycerol. The fractions for the nsp7 or nsp8 were collected, concentrated to about 10 mg ml^{-1} and stored at −80 °C until use.

Sf9 cells containing the coexpressed RdRp complex were resuspended in binding buffer of 25 mM HEPES pH 7.4, 300 mM sodium chloride, 25 mM imidazole, 1 mM magnesium chloride, 0.1% (v/v) IGEPALCA-630 (Anatrace), 1 mM tris(2-carboxyethyl)phosphine (TCEP), 10% (v/v) glycerol with additional EDTA-free Protease Inhibitor Cocktail (Bimake) and then incubated with agitation for 20 min at 4 °C. The incubated cells were lysed with a high-pressure homogenizer operating at 500 bar. The supernatant was isolated by centrifugation at 30,000*g* for 30 min, followed by incubation with Ni-NTA beads (GE Healthcare) for 2 h at 4 °C. After binding, the beads were washed with 20 column volumes of wash buffer of 25 mM HEPES, pH 7.4, 300 mM sodium chloride, 25 mM imidazole, 1 mM magnesium chloride, 1 mM TCEP and 10% (v/v) glycerol. The protein was eluted with 3–4 column volumes of elution buffer of 25 mM HEPES pH 7.4, 300 mM sodium chloride, 300 mM imidazole, 1 mM magnesium chloride, 1 mM TCEP and 10% (v/v) glycerol.

The coexpressed RdRp complex was incubated with additional nsp7 and nsp8 from the bacterial expression in a 1:1:2 molar ratio and incubated at 4 °C for 4 h. Incubated RdRp complex was concentrated with a 100 kDa molecular weight cut-off centrifugal filter unit (Millipore Corporation) and then size-separated by a Superdex 200 Increase 10/300 GL column in 25 mM HEPES pH 7.4, 300 mM sodium chloride, 1 mM magnesium chloride and 1 mM TCEP. The fractions for the monomeric complex were collected and concentrated to up to 12 mg ml^{-1}. Suramin sodium salt (purchased from MedChemExpress) was dissolved in water up to 50 mM. Suramin derivatives (purchased from TopScience) was dissolved in water at concentrations of 5 to 50 mM. For the suramin-bound complex, the concentrated RdRp complex at a concentration of 12 mg ml^{-1} were incubated with 0.8 mM suramin at 4 °C for 0.5 h for the next step of EM experiments.

Cryo-EM sample preparation and data acquisition. An aliquot of 3 µl of protein sample of suramin-bound complex (12 mg ml^{-1}) containing 0.0035% DDM was applied onto a glow-discharged 200 mesh grid (Quantifoil R1.2/1.3), blotted with filter paper for 3.0 s and plunge-frozen in liquid ethane using a FEI Vitrobot Mark IV. Cryo-EM micrographs were collected on a 300 kV Titan Krios microscope (FEI) equipped with a Gatan image filter (operated with a slit width of 20 eV) (GIF) and K3 direct detection camera. The microscope was operated at a calibrated magnification of ×46,773, yielding a pixel size of 1.069 Å on micrographs. In total, 11,846 micrographs in total were collected at an electron dose rate of 22.7 e^- Å^{-2} s^{-1} with a defocus range of −0.5 µm to −2.0 µm. Each video with an accumulated dose of 68 e^- Å^{-2} on sample were fractionated into a video stack of 36 image frames.

Image processing. Frames in each video stack were aligned for beam-induced motion correction using the program MotionCorr2 (ref. [24]). CTFFIND4 (ref. [25]) was used to determine the contrast transfer function (CTF) parameters. From this, 10,241 good micrographs were selected for further data processing. Auto-picking program of Relion 3.0 (ref. [26]) was used to pick the particles with the model of the apo–RdRp complex of COVID-19 (PDB ID 7BV1)[15] as a reference, yielding a total of 8,557,180 picked particles. Then, the extracted particle stack was transferred to software Cryosparc v.2 (ref. [27]) and a round of reference-free 2D classification was performed. Next, 3,159,808 particles were selected from classes representing projections of suramin-bound RdRp complex in different orientations and were subjected to two rounds of heterogenous refinement using a reconstruction of the apo–RdRp complex of COVID-19 (EMD-30209)[15] as a starting map. One converged three-dimensional (3D) class with a high-resolution feature contains one nsp12, one nsp7 and two copies of nsp8. The particles from that 3D class were then imported back into Relion 3.0 and subjected to a round of focused alignment with a mask including the whole protein components. Finally, 95,845 particles from a 3D class showing the highest resolution feature were selected for a round of 3D refinement. After a round of CTF refinement and Bayesian polishing of particles, another round of 3D refinement was performed, yielding a final reconstruction at a global resolution of 2.57 Å based on the gold-standard Fourier shell correlation (FSC) = 0.143 criterion[28]. The local resolution was calculated with Relion 3.0.

Model building. The model of suramin-bound RdRp complex was built by docking the model of apo structure of COVID-19 RdRp (PDB ID 7BV1) into the density map using UCSF Chimera[29], followed by ab initio model building of the N-terminal NiRAN domain of nsp12 and one copy of nsp8 in COOT[30], and real space refinement using real_space_refine program in PHENIX[31]. The model statistics were calculated with MolProbity[32] and listed in Table 1. Structural figures were prepared in Chimera or ChimeraX[33].

Preparation of template–primer RNA for polymerase assays. For the poly-A template–primer RNA, a short RNA oligonucleotide with sequence of 5′-FAM-GCUAUGUGAGAUUAAGUUAU-3′ (Sangon Biotech) was used as the primer strand and a longer RNA oligonucleotide with a sequence of 5′-AAAAAAAAAA AUAACUUAAUCUCACAUAGC-3′ (Sangon Biotech) was used as template strand. To anneal the RNA duplex, both oligonucleotides were mixed at equal molar ratio in annealing buffer (10 mM Tris-HCl, pH 8.0, 25 mM NaCl and 2.5 mM EDTA), denatured by heating to 94 °C for 5 min and then slowly cooled to room temperature. The poly-U template–primer RNA was prepared similar to poly-A with the sequences of 5′-FAM-GCUAUGUGAGAUUAAGUUAU-3′ and 5′-UUUUUUUUUUAUAACUUAAUCUCACAUAGC-3′.

Gel mobility shift assay to detect RNA–RdRp protein binding. A gel mobility shift assay was performed to detect the effect of tested compounds on RNA binding by the RdRp complex. The binding reaction contained 20 mM Tris-HCl 8.0, 10 mM KCl, 6 mM $MgCl_2$, 0.01% Triton-X100, 1 mM DTT, 1.14 U µl^{-1} RNase inhibitor (Vazyme Biotech), 9 µg of RdRp complex protein with 1 µg of poly-A template–primer RNA and increasing amounts of corresponding compounds (0, 1, 10, 100, 1,000 and 5,000 µM for suramin, and 0, 1, 10, 100, 1000, 5,000 and 10,000 µM for RDV-TP). Binding reactions were incubated for 30 min at room temperature and resolved on 4–20% native polyacrylamide gel (Thermo Fisher) running in 1× TBE buffer at 90 V for 1.5 h in a 4 °C cool room. The gel was imaged with a Tanon-5200 Multi Fluorescence Imager according to the manufacturer's protocol.

RdRp enzymatic activity assay and its inhibition by suramin. The purified SARS-CoV-2 RdRp complex from insect cell at final concentration of 1 µM was incubated with 3.0 µM poly-A template–primer RNA and 10 mM UTP(Macklin) in the presence of 1.14 U µl^{-1} RNase inhibitor in reaction buffer containing 20 mM Tris, pH 8.0, 10 mM KCl, 6 mM $MgCl_2$, 0.01% Triton-X100 and 1 mM DTT, which were prepared with DEPC-treated water. The total reaction volume was 20 µl. After incubation for 60 min in a 37 °C water bath, 40 µl of quench buffer (94% formamide, 30 mM EDTA, prepare with DEPC-treated water) was added to stop the reaction. A sample of 18 µl of reaction was mixed with 2 µl of 10× DNA loading buffer (Solarbio). Half of the sample (10 µl) was loaded onto a 10% urea–PAGE denatured gel, run at 120 V for 1 h, and imaged with a Tanon-5200 Multi Fluorescence Imager. The setup for the inhibition assays of the RdRp by suramin is identical to the above for the RdRp enzymatic assays, except that suramin was added to final concentrations of 0, 1, 2, 4, 8, 16 and 32 µM for 60 min before the addition of 10 mM UTP.

Fluorescence-based activity assay for SARS-CoV-2 RdRp. The detection of RNA synthesis by SARS-CoV-2 RdRp were established based on a real-time assay with the fluorescent dye SYTO 9 (Thermo Fisher), which binds double-stranded but not single-stranded RNA template molecules. The fluorescence emitted was recorded in real-time using a TECAN F200 with excitation and emission filters at 485 and 520 nm, respectively. The assay records the synthesis of dsRNA in a reaction using a poly-U molecule as a template and ATP as the nucleotide substrate, which has been adapted from methods previously documented for the detection of Zika virus polymerase activity[34]. Reactions were performed in individual wells of black 384-well low volume round bottom plates. The standard reaction contained 20 mM Tris-HCl, pH 8.0, 10 mM KCl, 6 mM $MgCl_2$, 180 µM ATP, 0.2 µM poly-U template–primer RNA, 0.01%Trition-X100,1 mM DTT,0.025 U ml^{-1} RNase

inhibitor (Vazyme Biotech) and 0.25 μM SYTO 9 (50 μM stock solution in TE buffer pH 7.5). The assay was initiated by the addition of 5 μg ml^{-1} SARS-CoV-2 RdRp and the fluorescence was recorded over 30 min at room temperature. The reaction with equivalent of dimethylsulfoxide (DMSO) was set as a maximum control, while the reaction with no SARS-CoV-2 RdRp was set as a minimum control. The reactions were carried out in the presence of 0.2 μM poly-U template–primer RNA and 180 μM ATP, and increasing concentrations of each inhibitor. Fluorometric results were expressed as mean ± s.d. Statistical significance was analyzed by two-way analysis of variance (ANOVA) using GraphPad Prism, v.8, as specified in the figure legends. K_m determinations were obtained by plotting the velocity of the reaction as a function of nucleotide or ssRNA template concentrations using nonlinear regression. IC_{50} values were obtained by fitting the velocity data to a four-parameter logistic equation. Kinetic parameters and IC_{50} values were calculated using Sigmaplot v.11.

Vero E6 cell-based antiviral assay for suramin and suramin derivatives. African green monkey kidney Vero E6 cell line was obtained from American Type Culture Collection (no. 1586) and maintained in Dulbecco's Modified Eagle Medium (Gibco Invitrogen) supplemented with 10% fetal bovine serum (Gibco Invitrogen), 1% antibiotic/antimycotic (Gibco Invitrogen), at 37 °C in a humidified 5% CO_2 incubator. A clinical isolate of SARS-CoV-2 (nCoV-2019BetaCoV/Wuhan/WIV04/2019) was propagated in Vero E6 cells that were tested free of mycoplasma contamination, and viral titer was determined by 50% tissue culture infective dose using immunofluorescence assay[16]. All the infection experiments were performed at biosafety level-3 (BSL-3).

Preseeded Vero E6 cells (5×10^4 cells per well) were incubated with the different concentrations of the indicated compounds for 1 h, and then were infected with SARS-CoV-2 at a multiplicity of infection of 0.01. Two hours later, the virus–drug mixture was removed and cells were further cultured with a fresh compound containing medium. At 24 h post infection, we measured viral RNA copy number in cell supernatant using real-time PCR[16]. Briefly, the viral RNA was extracted from the cell culture supernatant using the MiniBEST Viral RNA/DNA Extraction Kit (Takara, catalog no. 9766) according to the manufacturer's instructions. Then 3 μl total RNA was digested with genomic DNA eraser to remove contaminated DNA. In a 20 μl reaction system, the first-strand complementary DNA was synthesized, from which 2 μl of cDNA was used as a template for the next step of quantitative PCR. The primers used for quantitative PCR were RBD-qF1: 5′-CAATGGTTTAACAGGCACAGG-3′ and RBD-qR1: 5′-CTCAAGTGTCTGTGGATCACG-3′. The PCR amplification was performed as follows: 95 °C for 5 min followed by 40 cycles consisting of 95 °C for 15 s, 54 °C for 15 s and 72 °C for 30 s. DMSO was used in the controls. At least two independent experiments were carried out for each compound.

The cytotoxicity assay. The cytotoxicity of the tested drugs on Vero E6 were determined by CCK8 assays (Beyotime).

Statistical analysis. The IC_{50} values were expressed as mean ± s.d. from two independent experiments. The EC_{50} values were expressed as mean ± s.d. from three independent experiments. All values were determined via the nonlinear regression analysis using GraphPad Prism software v.8.0 (GraphPad Software).

Reporting Summary. Further information on research design is available in the Nature Research Reporting Summary linked to this article.

Data availability

EM density maps and atomic models have been deposited in the EMDB and PDB, respectively, with the accession codes EMD-30572 and PDB 7D4F. Source data are provided with this paper.

References

24. Zheng, S. Q. et al. MotionCor2: anisotropic correction of beam-induced motion for improved cryo-electron microscopy. *Nat. Methods* **14**, 331–332 (2017).
25. Rohou, A. & Grigorieff, N. CTFFIND4: fast and accurate defocus estimation from electron micrographs. *J. Struct. Biol.* **192**, 216–221 (2015).
26. Zivanov, J. et al. New tools for automated high-resolution cryo-EM structure determination in RELION-3. *eLife* **7**, e42166 (2018).
27. Punjani, A., Rubinstein, J. L., Fleet, D. J. & Brubaker, M. A. cryoSPARC: algorithms for rapid unsupervised cryo-EM structure determination. *Nat. Methods* **14**, 290–296 (2017).
28. Rosenthal, P. B. & Henderson, R. Optimal determination of particle orientation, absolute hand, and contrast loss in single-particle electron cryomicroscopy. *J. Mol. Biol.* **333**, 721–745 (2003).
29. Pettersen, E. F. et al. UCSF chimera—a visualization system for exploratory research and analysis. *J. Comput. Chem.* **25**, 1605–1612 (2004).
30. Emsley, P. & Cowtan, K. Coot: model-building tools for molecular graphics. *Acta Crystallogr. Sect. D. Biol. Crystallogr.* **60**, 2126–2132 (2004).
31. Adams, P. D. et al. PHENIX: a comprehensive Python-based system for macromolecular structure solution. *Acta Crystallogr. D. Biol. Crystallogr.* **66**, 213–221 (2010).
32. Chen, V. B. et al. MolProbity: all-atom structure validation for macromolecular crystallography. *Acta Crystallogr. D. Biol. Crystallogr.* **66**, 12–21 (2010).
33. Goddard, T. D. et al. UCSF ChimeraX: meeting modern challenges in visualization and analysis. *Protein Sci.* **27**, 14–25 (2018).
34. Saez-Alvarez, Y., Arias, A., Del Aguila, C. & Agudo, R. Development of a fluorescence-based method for the rapid determination of Zika virus polymerase activity and the screening of antiviral drugs. *Sci. Rep.* **9**, 5397 (2019).

Acknowledgements

The cryo-EM data were collected at the Cryo-Electron Microscopy Research Center, Shanghai Institute of Materia Medica. This work was partially supported by the National Key R&D Program of China (grant no. 2020YFC0861000), CAMS Innovation Fund for Medical Sciences grant no. 2020-I2M-CoV19-001 and Tsinghua University-Peking University Center for Life Sciences grant no. 045-160321001 to S.Z.; the National Key R&D Programs of China grant no. 2018YFA0507002; Shanghai Municipal Science and Technology Major Project grant no. 2019SHZDZX02 and the Strategic Priority Research Program of Chinese Academy of Sciences XDB37030103 to H.E.X.; the CAS Young Innovator Association award to W.Y.; the 100 Talents Program of the Chinese Academy of Sciences, Chinese Academy of Sciences (grant no. XDA12010317), Natural Science Foundation of Shanghai (grant no. 18ZR1447700) to X.Y.; the National Natural Science Foundation of China (grant no. 31900869) and Shanghai Sailing Program (grant no. 19YF1456800) to Z.L.; Science and Technology Commission of Shanghai Municipal grant no. 20431900100 and Jack Ma Foundation grant no. 2020-CMKYGG-05 to H.J.; National Natural Science Foundation grant no. 31770796, National Science and Technology Major Project grant no. 2018ZX09711002, and K.C. Wong Education Foundation to Y.J., the National Natural Science Foundation of China (grant no. 31970165) to L.Z. and by the National Natural Science Foundation of China (grant no. 81903433) to J.S.

Author contributions

W.Y. designed the expression constructs, purified the RdRp complex, prepared samples and cryo-EM grids, performed data collection and processing toward the structure determination, analyzed the structures and prepared figures and manuscript. X.L. designed RdRp activity assays and discovered RdRp inhibition by suramin, participated in data interpretation and figure preparation. Z.L., Z.Z., Q.W. and X.Y. evaluated the specimen by negative-stain EM, screened the cryo-EM conditions, prepared the cryo-EM grids and collected cryo-EM images, and performed data processing, density map calculations, model building and figure preparation. L.Z., Q.W. and G.X. designed and performed cell-based viral inhibition assays. X.W., F.Z. and M.G. participated in expression, purification and functional assays of the RdRp. J.S., E.Y. and M.L. participated in the analysis of suramin derivatives. Y.J. participated in experimental design and manuscript editing. H.J. conceived and coordinated the project. S.Z. conceived the project, initiated collaboration with H.E.X. and supervised X.L. H.E.X. conceived and supervised the project, analyzed the structures and wrote the manuscript with inputs from all authors.

Competing interests

The authors declare no competing interests.

Additional information

Extended data is available for this paper at https://doi.org/10.1038/s41594-021-00570-0.

Supplementary information The online version contains supplementary material available at https://doi.org/10.1038/s41594-021-00570-0.

Correspondence and requests for materials should be addressed to L.Z., X.Y., S.Z. or H.E.X.

Peer review information *Nature Structural and Molecular Biology* thanks the anonymous reviewers for their contribution to the peer review of this work. Peer reviewer reports are available. Anke Sparmann was the primary editor on this article and managed its editorial process and peer review in collaboration with the rest of the editorial team.

Reprints and permissions information is available at www.nature.com/reprints.

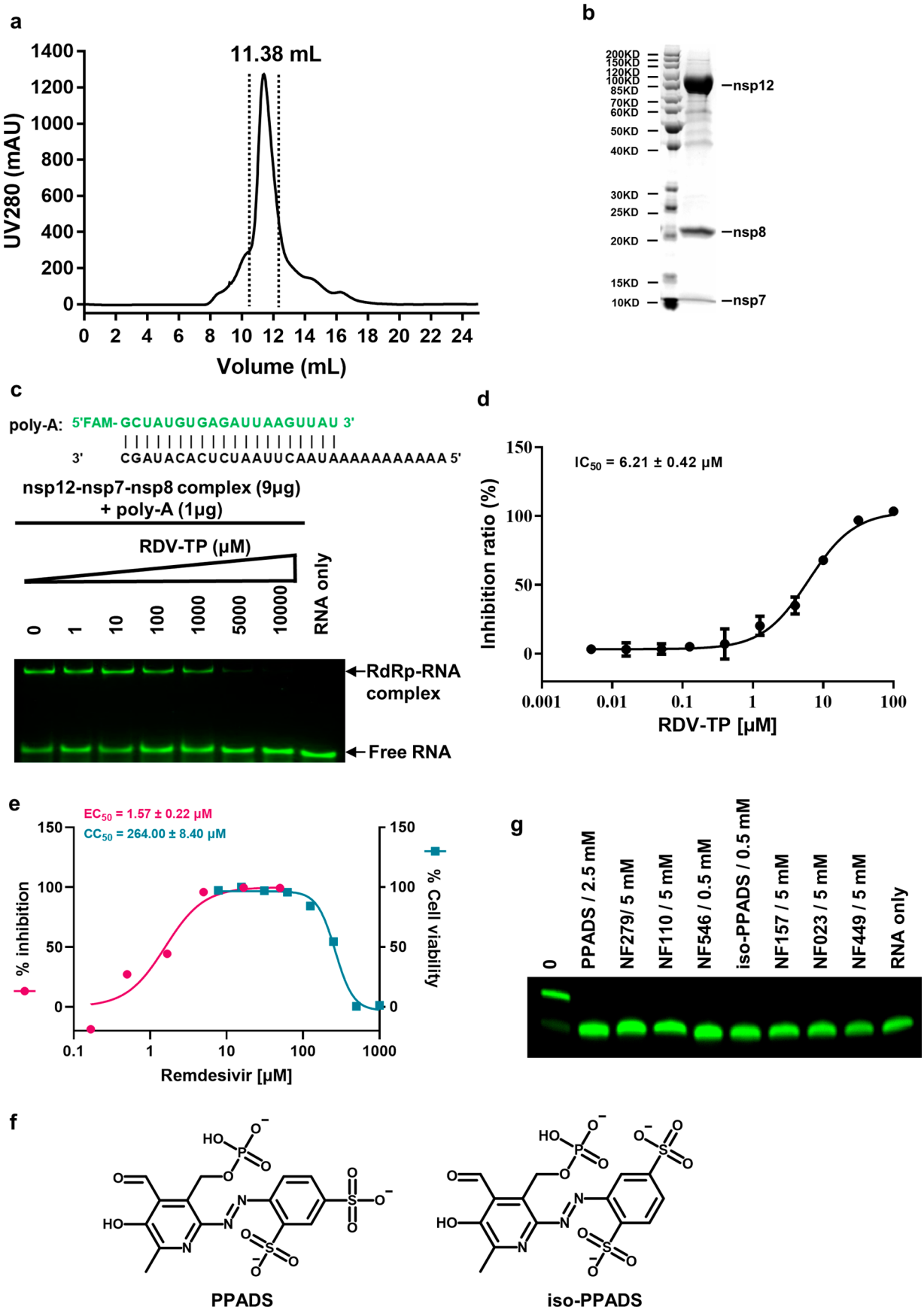

Extended Data Fig. 1 | See next page for caption.

Extended Data Fig. 1 | Purification and characterization of the RdRp complex. a, Gel filtration profile of the RdRp complex with nsp7 and nsp8. **b**, SDS gel of the purified RdRp complex with nsp7 and nsp8. **c**, Gel mobility shift of the RdRp-RNA complex and the effect of RDV-TP. **d**, IC_{50} of RDV-TP for the RdRp complex, determined by two independent experiments and error bars means s.d. of the data. **e**, EC_{50} of remdesivir for SARS-CoV-2 inhibition and CC_{50} of remdesivir for cell-based toxicity, determined by three independent experiments and error bars means s.d. of the data. **f**, The structures of PPADS and iso-PPADS. **g**, Elongation of partial RNA duplex by the purified RdRp complex and its inhibition by 9 suramin derivatives at 0.5-5.0 mM concentrations depending on the solubility of each compound.

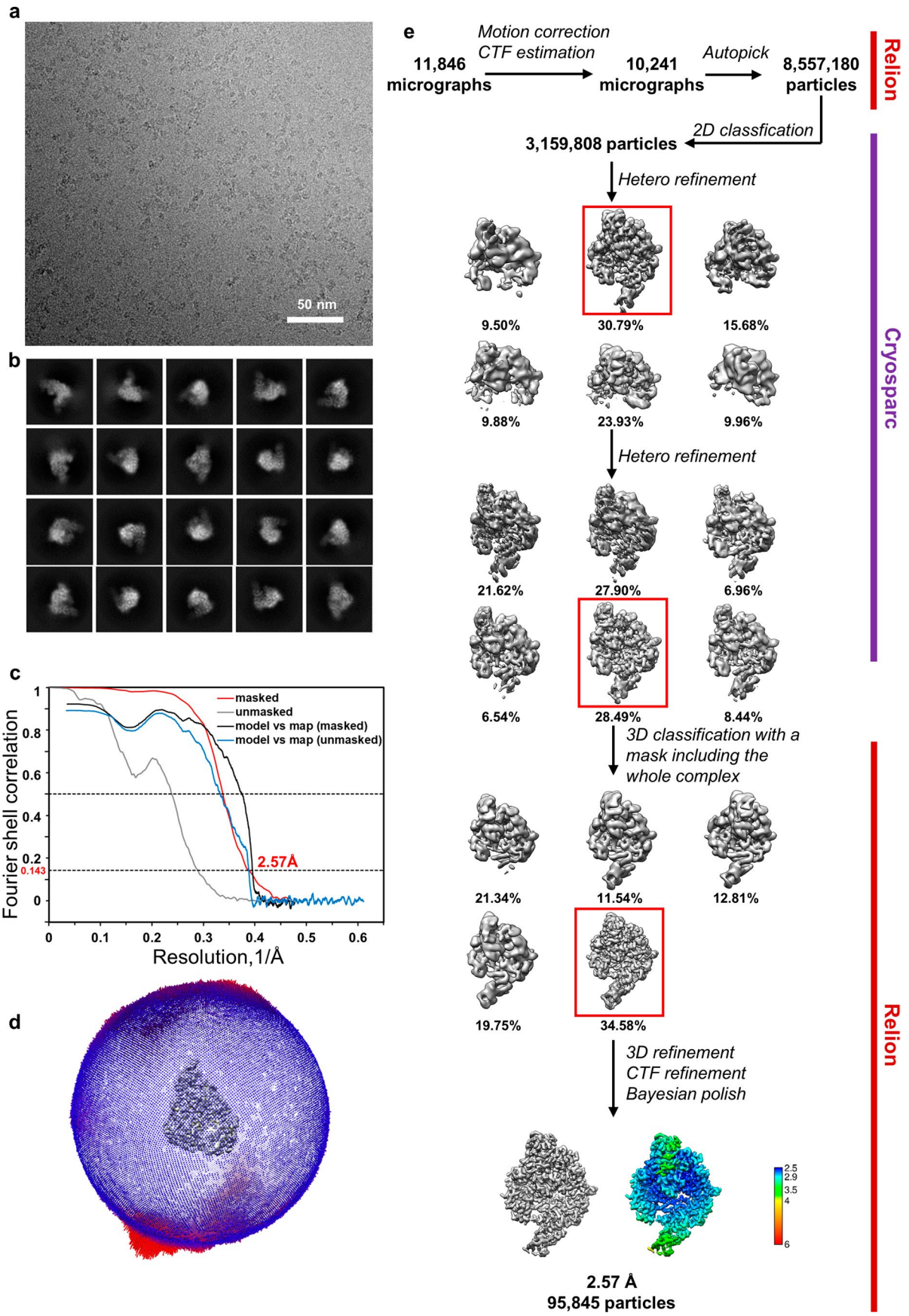

Extended Data Fig. 2 | See next page for caption.

Extended Data Fig. 2 | Single particle cryo-EM analysis of the RdRp-suramin complex. a, Representative cryo-EM micrograph of the RdRp-suramin complex. **b**, Representative 2D class averages of the RdRp-suramin complex. **c**, Fourier shell correlation curves of cryo-EM map for the suramin-RdRp complex. **d**, Euler angle distribution of particles used in the final reconstruction. **e**, Flowchart of cryo-EM works of the suramin-RdRp complex with maps colored by local resolution (Å).

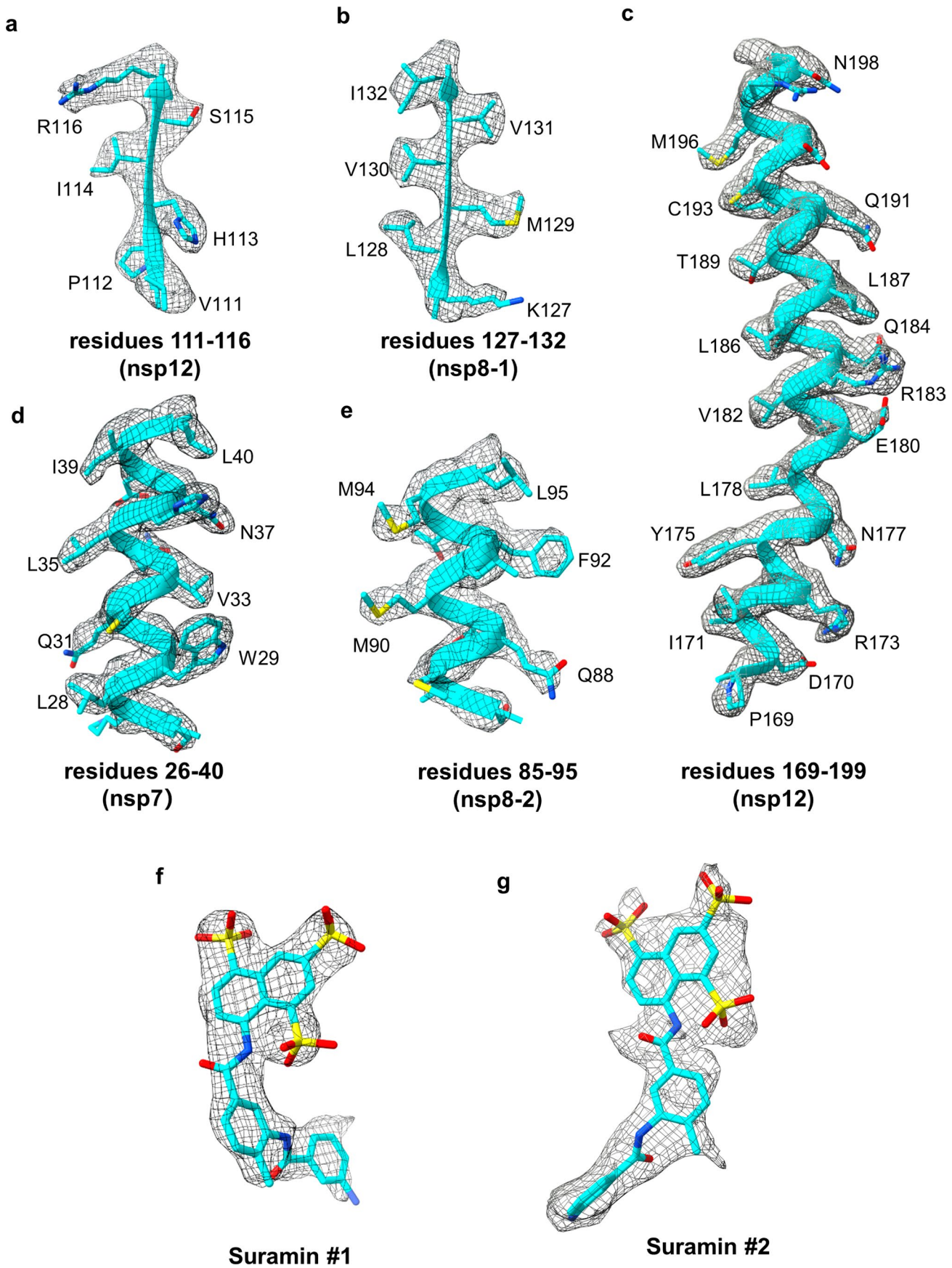

Extended Data Fig. 3 | See next page for caption.

Extended Data Fig. 3 | Cryo-EM map for the RdRp in complex with suramin. a-g, Cryo-EM map and model of nsp12 (residues 111-116, contour σ level: 4σ) (A), nsp8-1 (residues 127-132, contour σ level: 6σ) (B), nsp12 (residues 169-199, contour σ level: 6σ) (C), nsp7 (residues 26-40, contour σ level: 6σ) (D), nsp8-2 (residues 85–95, contour σ level: 5σ) (E), and the two bound suramin molecules (F and G, suramin#1, contour σ level: 5.5σ; suramin#2, contour σ level: 3.5σ).

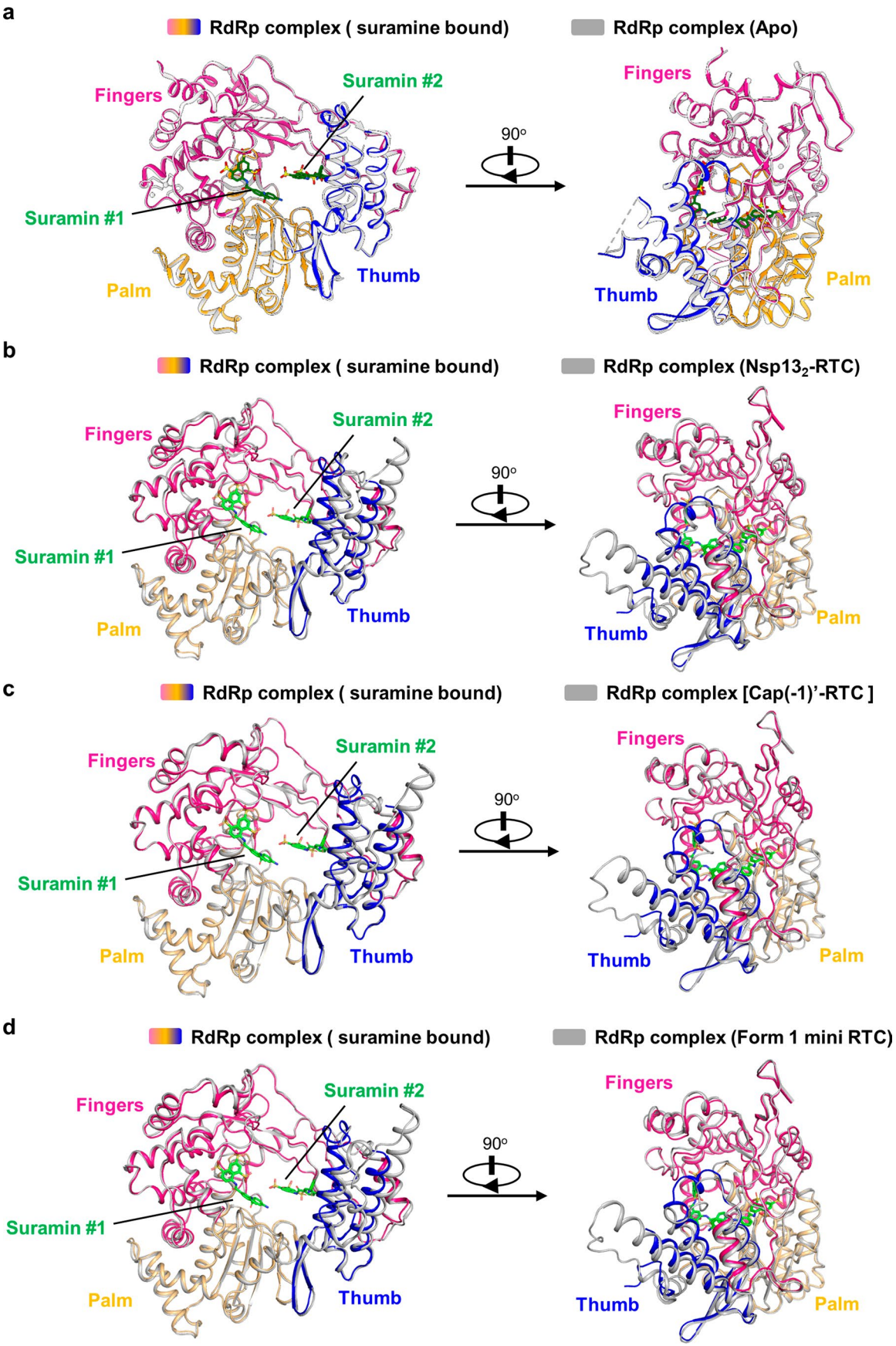

Extended Data Fig. 4 | See next page for caption.

Extended Data Fig. 4 | Structural comparisons of the SARS-CoV-2 RdRp-suramin structure with the apo–RdRp structure and other structures of replication/transcription complex (RTC). Overall views of the RdRp-suramin structure overlapped with the apo RdRp structure (PDB ID: 7BV1) in panel a; the nsp132-RTC structure (PDB ID: 6XEZ) in panel b; the cap (-1)'-RTC structure (PDB ID: 7CYQ) in panel c; and the form 1 mini RTC structure (PDB ID: 7CXM) in panel d. For clarity, only the polymerase domains are shown. The thumb, palm and fingers domains of the RdRp of the SARS-CoV-2 RdRp-suramin structure are in blue, orange and red, respectively, with the two suramin molecules in green. The other RdRp complex structures are in light gray.

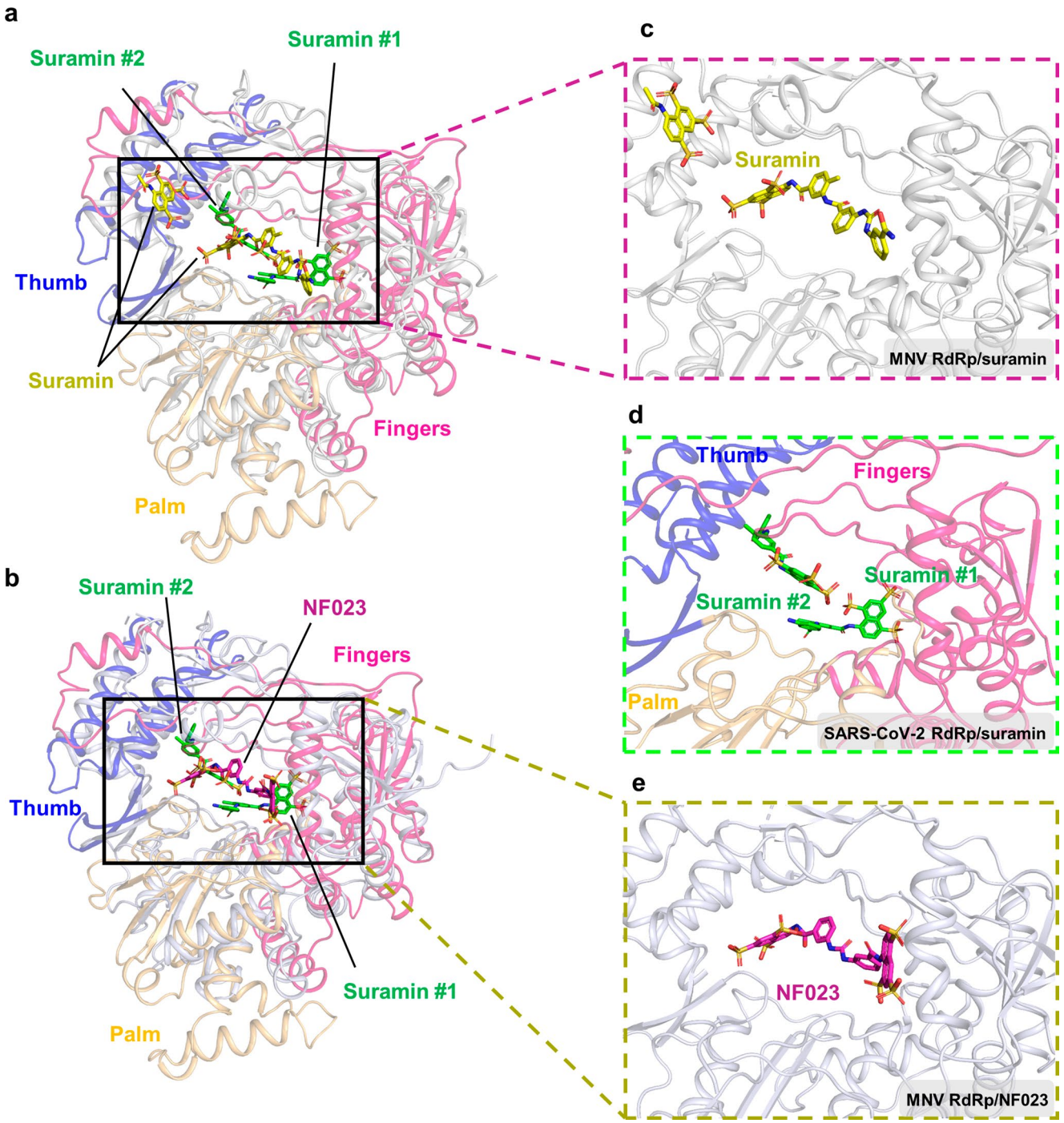

Extended Data Fig. 5 | Comparison of SARS-CoV-2 RdRp-suramin complex with MNV (Murine Noroviruses) RdRp-suramin complex and MNV RdRp-NF023. a, Superimposition of the SARS-CoV-2 RdRp-suramin structure with the MNV RdRp-suramin structure (PDB ID: 3UR0) based on the polymerase domain. Only the polymerase domain of SARS-CoV-2 RdRp is shown. RdRp in MNV RdRp-suramin structure is in light gray with the two suramin molecules in yellow. The thumb, palm and fingers domains in the RdRp of SARS-CoV-2 RdRp-suramin structure are in blue, orange and red, respectively, with the two suramin molecules in green. **b**, Superimposition of SARS-CoV-2 RdRp-suramin structure with MNV RdRp-NF023 structure (PDB ID: 3URF) based on the polymerase domain. The RdRp in MNV RdRp-NF023 structure is in light gray with the NF023 molecule in magenta. The thumb, palm and fingers domains in the RdRp of SARS-CoV-2 RdRp-suramin structure are in blue, orange and red, respectively, with the two suramin molecules in green. **c**, A close view of the suramin within the catalytic site in the MNV RdRp-suramin structure, color code as in panel a. **d**, A close view of the suramin within the catalytic site in the SARS-CoV-2 RdRp-suramin structure, color code as in panels a and b. **e**, A close view of the NF023 within the catalytic site in the MNV RdRp-NF023 structure, color code as in panel b.

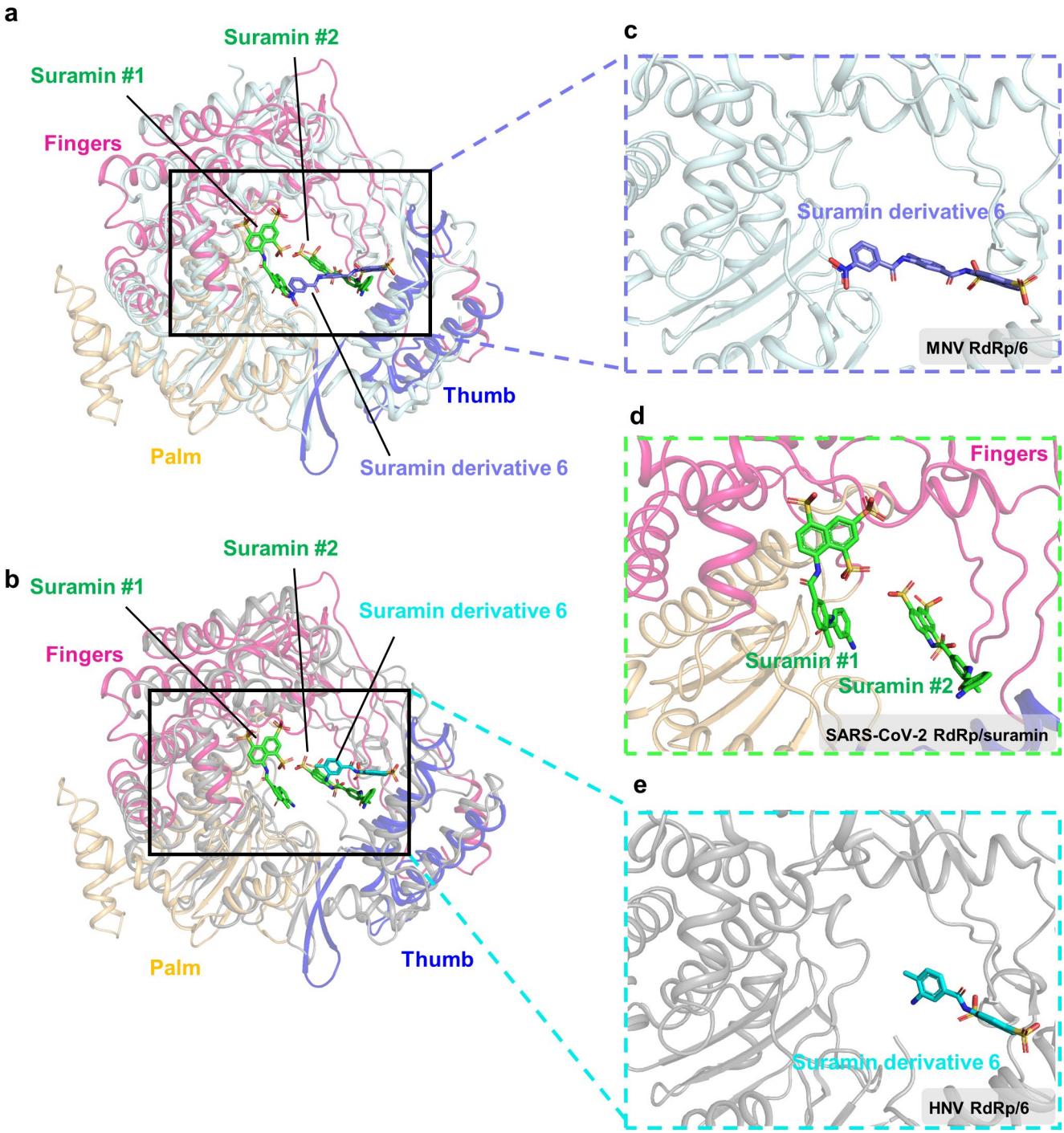

Extended Data Fig. 6 | Comparison of SARS-CoV-2 RdRp-suramin complex with MNV RdRp-suramin derivative 6 complex and HNV (Human Noroviruses) RdRp-suramin derivative 6. a, Superimposition of SARS-CoV-2 RdRp-suramin structure with MNV RdRp-suramin derivative 6 structure (PDB ID: 4NUR) based on the polymerase domain. Only the polymerase domain of SARS-CoV-2 RdRp is shown. The RdRp in MNV RdRp-6 structure is in light gray with the suramin derivative 6 molecule in light blue. The thumb, palm and fingers domains in the RdRp of SARS-CoV-2 RdRp-suramin structure are in blue, orange and red, respectively, with the two suramin molecules in green. **b**, Superimposition of SARS-CoV-2 RdRp-suramin structure with HNV RdRp-suramin derivative 6 structure (PDB ID: 4NRT) based on the polymerase domain. The RdRp in HNV RdRp-6 structure is in light gray with suramin derivative 6 in cyan. The thumb, palm and fingers domains in the RdRp of SARS-CoV-2 RdRp-suramin structure are in blue, orange and red, respectively, with the two suramin molecules in green. **c**, A close view of the suramin derivative 6 within the active site in the MNV RdRp-suramin derivative 6 structure, the color code is used as in panel a. **d**, A close view of the suramin within the active site in the SARS-CoV-2 RdRp-suramin structure, the color code is used as in panels a and b. **e**, A close view of the suramin derivative 6 within the active site in the HNV RdRp-suramin derivative 6 structure, the color code is used as in panel b.

nature research

Corresponding author(s): H. Eric Xu (eric.xu@simm.ac.cn)

Last updated by author(s): Nov 1, 2020

Reporting Summary

Nature Research wishes to improve the reproducibility of the work that we publish. This form provides structure for consistency and transparency in reporting. For further information on Nature Research policies, see our Editorial Policies and the Editorial Policy Checklist.

Statistics

For all statistical analyses, confirm that the following items are present in the figure legend, table legend, main text, or Methods section.

n/a	Confirmed
☐	☒ The exact sample size (*n*) for each experimental group/condition, given as a discrete number and unit of measurement
☐	☒ A statement on whether measurements were taken from distinct samples or whether the same sample was measured repeatedly
☒	☐ The statistical test(s) used AND whether they are one- or two-sided *Only common tests should be described solely by name; describe more complex techniques in the Methods section.*
☒	☐ A description of all covariates tested
☒	☐ A description of any assumptions or corrections, such as tests of normality and adjustment for multiple comparisons
☐	☒ A full description of the statistical parameters including central tendency (e.g. means) or other basic estimates (e.g. regression coefficient) AND variation (e.g. standard deviation) or associated estimates of uncertainty (e.g. confidence intervals)
☒	☐ For null hypothesis testing, the test statistic (e.g. *F*, *t*, *r*) with confidence intervals, effect sizes, degrees of freedom and *P* value noted *Give P values as exact values whenever suitable.*
☒	☐ For Bayesian analysis, information on the choice of priors and Markov chain Monte Carlo settings
☒	☐ For hierarchical and complex designs, identification of the appropriate level for tests and full reporting of outcomes
☒	☐ Estimates of effect sizes (e.g. Cohen's *d*, Pearson's *r*), indicating how they were calculated

Our web collection on statistics for biologists contains articles on many of the points above.

Software and code

Policy information about availability of computer code

Data collection	SerialEM v3.7
Data analysis	Relion v3.0, Cryosparc v2.15, MotionCor2 v1.2.2 , CTFFIND4, PHENIX-1.14_3260, Coot 0.8.9.1, ChimeraX 1.0, GraphPad Prism 8.3.0, CLUSTAL 2.1, Pymol 2.4.0

For manuscripts utilizing custom algorithms or software that are central to the research but not yet described in published literature, software must be made available to editors and reviewers. We strongly encourage code deposition in a community repository (e.g. GitHub). See the Nature Research guidelines for submitting code & software for further information.

Data

Policy information about availability of data

All manuscripts must include a data availability statement. This statement should provide the following information, where applicable:

- Accession codes, unique identifiers, or web links for publicly available datasets
- A list of figures that have associated raw data
- A description of any restrictions on data availability

The atomic coordinates of the the SARS-CoV-2 RdRp bound to suramin have been deposited in the Protein Data Bank (http://www.rcsb.org) under the accession code 7D4F. The density map has been deposited in the Electron Microscopy Data Bank (https://www.ebi.ac.uk/pdbe/emdb/) with the accession code EMD-30572. All other data are available from the corresponding author upon reasonable request. Correspondence and requests for materials should be addressed to H. Eric Xu (eric.xu@simm.ac.cn).

Field-specific reporting

Please select the one below that is the best fit for your research. If you are not sure, read the appropriate sections before making your selection.

☒ Life sciences ☐ Behavioural & social sciences ☐ Ecological, evolutionary & environmental sciences

For a reference copy of the document with all sections, see nature.com/documents/nr-reporting-summary-flat.pdf

Life sciences study design

All studies must disclose on these points even when the disclosure is negative.

Sample size	No statistical method was used to determine sample size.
Data exclusions	No data was excluded.
Replication	For the biochemical assay, each experiment was replicated for 3 times and the results were reproduced each time.
Randomization	The independent variables of the experimental design were well controlled and did not require randomization
Blinding	Experimental result s were all quantitative and did not require any subjective analysis, thus no experiments were preformed with blinding

Reporting for specific materials, systems and methods

We require information from authors about some types of materials, experimental systems and methods used in many studies. Here, indicate whether each material, system or method listed is relevant to your study. If you are not sure if a list item applies to your research, read the appropriate section before selecting a response.

Materials & experimental systems

n/a	Involved in the study
☒	☐ Antibodies
☐	☒ Eukaryotic cell lines
☒	☐ Palaeontology and archaeology
☒	☐ Animals and other organisms
☒	☐ Human research participants
☒	☐ Clinical data
☒	☐ Dual use research of concern

Methods

n/a	Involved in the study
☒	☐ ChIP-seq
☒	☐ Flow cytometry
☒	☐ MRI-based neuroimaging

Eukaryotic cell lines

Policy information about cell lines

Cell line source(s)	African green monkey kidney Vero E6 cells (ATCC-1586)
Authentication	No further authentication was performed for commercially available cell lines.
Mycoplasma contamination	No mycoplasma contamination.
Commonly misidentified lines (See ICLAC register)	No commonly misidentified cell lines were used.